Contents lists available at Science-Gate

International Journal of Advanced and Applied Sciences

Journal homepage: http://www.science-gate.com/IJAAS.html

Wave drag coefficient of nonaxisymmetric irregular-shaped bodies

Sabina Serdarevic-Kadic *

Mechanical Engineering Faculty, University of Sarajevo, Sarajevo, Bosnia and Herzegovina

ARTICLE INFO

Article history:
Received 28 April 2022
Received in revised form
20 July 2022
Accepted 2 September 2022

Keywords:
Wave drag coefficient
Flow field
Pressure
Mach number

ABSTRACT

At high speeds, transonic and supersonic, the wave drag coefficient is a significant part of drag coefficients and it depends on the front surface shape and flow velocity. Drag, wave drag, drag coefficient, and wave drag coefficient for four bodies with the same width, height and length, and different shapes are estimated by CFD (ANSYS Fluent). For different front surface curvatures, at high flow velocity, pressure distribution on the front surface of the body, and flow field as a contour of Mach number are analyzed. The influence of front surface curvature on detached shock wave distance is determined.

1. Introduction

Aerodynamic force is exerted on a body whenever there is a relative velocity between the body and the air. There are only two basic sources of aerodynamic force: The pressure distribution and the frictional shear stress distribution exerted by the airflow on the body surface. The pressure and shear stress acting at each point on the body surface. The pressure exerted by the air at a point on the surface acts perpendicular to the surface at that point and the shear stress acts tangentially to the surface at that point. The distribution of pressure and shear stress represents a distributed load over the surface. The net aerodynamic force on the body is due to the net imbalance between these distributed loads as they are summed (integrated) over the entire surface (Anderson, 2017). Pressure distribution over the body is dependent on flow velocity and shape of the body. If the flow velocity is near or greater than the speed of sound (transonic and supersonic flows), aerodynamic force in the velocity direction at the wet surface of the body is called wave drag. Transonic and supersonic flows around the body are characterized by the presence of shock waves.

There are papers about the total drag coefficient of fragments (irregular-shaped bodies) from experimental data. McCleskey (1988) calculated the drag coefficient from individual test records for 96 irregular-shaped bodies (fragments) tested in the vertical wind tunnel at low subsonic speed. Additionally, he proposed a model where the drag, as a function of the Mach number, is constructed from the subsonic anchor point and pivot points for transonic and supersonic regimes taken from other research works. Miller (1990) described the initial results of wind tunnel and air gun tests to measure the drag coefficients of representative bomb and projectile fragments over the entire Mach number range experienced in flight. The drag coefficient of fragment number 60 from McCleskey (1988) as a function of Mach number at transonic and supersonic speeds showed a somewhat higher value than established theoretically by McCleskey (1988).

Twisdale and Vickery (1992) applied modified cross-flow theory to develop the expression for the drag coefficient of the random orientation rectangular parallelepiped as a function of orientation angles and geometrical characteristics.

Moxnes et al. (2017) showed different novel analytical models for the expected projected area and drag coefficient of fragments that tumble or rotate with the rotational axis normal to the velocity vector. They forecasted a model where the expected drag coefficient depends on the shape and Mach number. Murman (2010) presented a method for predicting the drag of unconstrained bluff bodies from subsonic through supersonic flight conditions using analytic expressions.

Moore (2000) proposed that the best way to analyze the wave drag of a noncircular body would be through numerical computations using code such as full Euler or Navier-Stokes because the wave drag is more complicated than the other two components due to the fact that it is a function of the slope along the body surface as well as the area distribution.

Research works about body wave drag of irregular nonaxisymmetric body shapes which is

* Corresponding Author.
Email Address: serdarevic@mef.unsa.ba
https://doi.org/10.21833/ijaas.2022.12.013
Corresponding author's ORCID profile:
https://orcid.org/0000-0003-3163-501X

dominant in the supersonic regime have not been found in the available literature.

The purpose of this study is to determine the quote of wave drag coefficient in the drag coefficient of an irregular-shaped body, as well as its dependence on front area shape and its curvature and flow velocity, for Mach numbers from 1 to 2.

2. Drag coefficient

A component of aerodynamic force parallel to freestream velocity is called drag force. The drag force is defined in terms of this drag coefficient:

$$D = \frac{1}{2}\rho_\infty V_\infty^2 A_{ref} C_D \quad (1)$$

where, $\rho_\infty$is freestream density, V_∞ is freestream velocity, A_{ref} is reference area and C_D is the aerodynamic drag coefficient. The reference area is chosen to pertain to the given geometric body shape.

If it is assumed that the outer surface of the body in airflow consists of a wet surface S_w (surface in contact with air) and dry surface S_d, then the drag coefficient can be written as:

$$C_D = C_{D_w} + C_{D_{sf}} + C_{D_r} \quad (2)$$

where, $C_{D_w}$is pressure drag coefficient due to wet surface, $C_{D_{sf}}$ is skin friction drag due to wet surface and C_{D_r} is pressure drag coefficient due to the dry surface (rear surface).

In front of a blunt body in supersonic flow a detached shock wave (curved bow shock) is generated as shown in Fig. 1. At point *a*, the shock wave is normal to the upstream flow; hence, point *a* corresponds to a normal shock wave. Away from point *a*, the shock wave gradually becomes curved and weaker (Anderson, 2017).

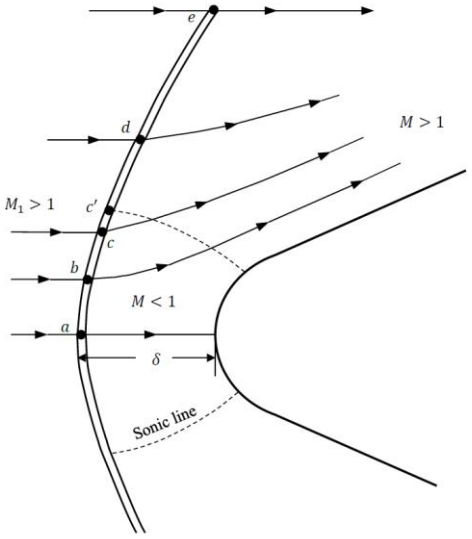

Fig. 1: Flow over a supersonic blunt body (Anderson, 2017; Catovic et al., 2018)

The shape of the detached shock wave, its detachment distance, and the complete flow field between the shock and the body depends on the upstream Mach number and the size and shape of the body (Anderson, 2017).

Maximum pressure on a wet surface is generated in the region behind the normal part of the curved bow shock and can be determined from the following relations:

- Pressure behind normal shock wave:

$$\frac{p}{p_\infty} = 1 + \frac{2\gamma}{\gamma+1}(M_\infty^2 - 1) \quad (3)$$

- Mach number behind normal shock wave:

$$M^2 = \frac{1+[(\gamma-1)/2]M_\infty^2}{\gamma M_\infty^2 - (\gamma-1)/2} \quad (4)$$

- Stagnation pressure behind a normal shock wave is the maximum pressure on the body:

$$\frac{p_0}{p} = \left(1 + \frac{\gamma-1}{2}M^2\right)^{\frac{\gamma}{\gamma-1}} \quad (5)$$

where, p_∞ is freestream pressure, $M_\infty$is freestream Mach number, p is pressure behind the normal shock wave, M is Mach number behind the normal shock wave, p_0 is pressure on the surface and $\gamma = 1,4$ for air.

3. Methodology

In this study, 4 nonaxisymmetric irregular-shaped bodies are taken under consideration: Three-axis ellipsoid (ellipsoid), short cylinder with elliptic-shaped base (short elliptic cylinder), long cylinder with elliptic-shaped base (long elliptic cylinder) and parallelepiped. These bodies have the same dimensions: Width $a = 68\ mm$, height $b = 17{,}3\ mm$ and length $c = 12\ mm$ and they are shown in Fig. 2. Ellipsoid and short elliptic cylinder have a reference area $A_{ref} = \frac{ab}{4}\pi$, and parallelepiped and the long elliptic cylinder has a reference area $A_{ref} = ab$. Body dimensions are chosen because drag force values of a three-axis ellipsoid with the same dimensions are available. The choice of body shape is made with the purpose of noticing the influence of a flat surface, curved surface, and sharp edge on the wave drag coefficient.

Numerical simulation of the flow field around bodies is obtained with the computational fluid dynamics software ANSYS Fluent. The following is adopted for all simulations:

- The working fluid is air, an ideal gas, which is modified in accordance with compressibility and changes in thermophysical characteristics with temperature. Density and viscosity depend on temperature and c_p and thermal conductivity are considered constants.
- Pressure and temperature of air free flow correspond to parameters of air at sea level according to the standard atmosphere ICAO, $p_\infty = 101325\ Pa$ and $T_\infty = 288\ K$.

- The direction of airflow is assumed to be perpendicular to the maximum cross-section of the body (reference area).
- Flow around the body is compressible and turbulent.
- The spatial domain is divided into two parts, inner and outer. Discretization of the spatial domain inner part is performed by non-uniform unstructured mesh and discretization of the spatial domain outer part is performed by non-uniform structured mesh, as shown in Fig. 3.
- A numerical method that simultaneously solves the equation of continuity, equation of momentum and energy equation is used. This method is developed for high-velocity compressible flows.
- The governing equations are linearized in an implicit manner. For a given variable, the unknown value in each cell is computed using a relation that includes both existing and unknown values from neighboring cells. Therefore, each unknown variable will appear in more than one equation in the system, and these equations must be solved simultaneously to give the unknown quantities.
- The Spalart-Allmaras model (Spalart and Allmaras, 1992) is selected for turbulence modeling.

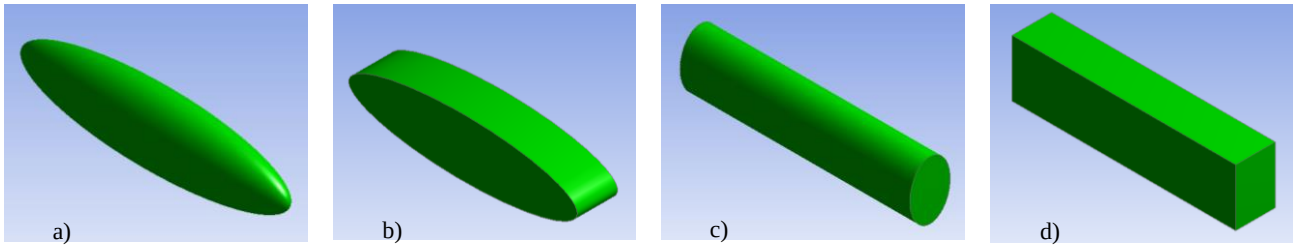

Fig. 2: Irregular-shaped bodies: a) three-axis ellipsoid; b) short elliptic cylinder; c) long elliptic cylinder; d) parallelepiped

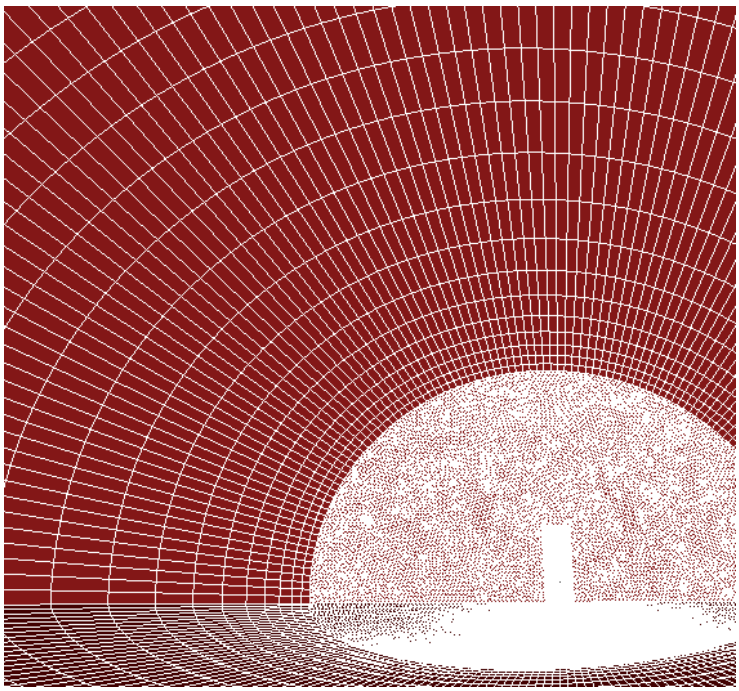

Fig. 3: Discretization of spatial domain

Chosen bodies have three planes of symmetry and expected flow images are symmetrical to two planes, so the simulations were made on one-quarter of the body with the purpose of decreasing the number of mesh cells and time of calculation.

The computational domain is limited to the body contour, two symmetry planes, and outer boundary. The radius of the outer boundary is more than 10 times the body's maximum dimension.

The following types of the boundary are chosen:

- "Wall" boundary, which is used to delimit the regions of fluid and solid, is set to body contour.
- "Symmetry" boundaries are used as symmetry planes.
- "Pressure far field" boundary, which is used for modeling compressible free flow parameters at infinity, is set on the outer boundary of the computation domain.

The solution of Navier-Stokes equations was done by using a 3-dimensional density-based solver. The Wall boundary of an ellipsoid and the wall boundary of a long elliptic cylinder are divided into 2 parts: The front surface and rear surface by maximum cross-section during geometry modeling. The exterior surfaces of the short elliptic cylinder and parallelepiped are divided into 3 parts: The front surface, the middle section surface, and the rear surface.

The verification of the model was made on the basis of a three-axis ellipsoid drag force (Kljuno and Catovic, 2019). The deviation of results is not greater than 3.5%. The most important reasons for the deviation of results are different free flow temperature, different mesh, and different radii of the outer boundary. Twenty simulations were made, five for each body. Simulations were made for $M = 1; 1.2; 1.5; 1.8$ and 2.

4. Results and discussion

The drag force coefficient has three components which are generated by the pressure of the air as it is compressed on the body surface, the friction of the air as it passes over the body, and the pressure on the after body by the separation of the flow from the body surface. All of the individual drag force components are computed simultaneously as part of the solution.

According to the geometry of the body and division into the front, middle section, and rear surface, for each part of the body, drag force due to pressure and drag force due to shear stress are estimated and shown in the Fluent force report for the direction vector of flow velocity. Drag force is a sum of drag forces due to pressure and shear stress for all parts of a body. Drag force at the front surface due to pressure is in fact wave drag force.

Drag force coefficient and wave drag coefficient are calculated by the definition of aerodynamic force coefficient which follows from Eq. 1 and for the value of reference area which is entered as reference value during the problem setup in Fluent.

The simulation results are grouped according to the maximum cross-section area of the bodies.

Values of drag force D, wave drag force D_w, aerodynamic drag coefficient C_D and aerodynamic wave drag coefficient C_{D_w} as a function of the Mach number for ellipsoid and short elliptic cylinder are shown in Table 1, and these values for parallelepiped and long elliptic cylinder are shown in Table 2.

Table 1: Drag and drag coefficient as a function of Mach number for ellipsoid and short elliptic cylinder by CFD

Mach No.	Ellipsoid				Short elliptic cylinder			
	D [N]	D_W [N]	C_D	C_{Dw}	D [N]	D_W [N]	C_D	C_{Dw}
1	94.57	46.42	1.444	0.7095	114.61	74.30	1.750	1.1346
1.2	141.23	83.48	1.498	0.8853	168.89	119.41	1.791	1.2663
1.5	219.72	153.38	1.491	1.0410	265.76	207.25	1.804	1.4066
1.8	310.86	239.48	1.465	1.1287	380.34	315.79	1.793	1.4884
2	378.63	305.44	1.445	1.1661	458.91	391.61	1.752	1.4950

Table 2: Drag and drag coefficient as a function of Mach number for long elliptic cylinder and parallelepiped by CFD

Mach No.	Parallelepiped				Long elliptic cylinder			
	D [N]	D_W [N]	C_D	C_{Dw}	D [N]	D_W [N]	C_D	C_{Dw}
1	147.48	93.64	1.768	1.1231	126.80	63.23	1.521	0.7583
1.2	214.57	150.93	1.787	1.2571	182.34	108.66	1.544	0.9203
1.5	338.42	262.21	1.804	1.3977	288.59	203.60	1.538	1.0853
1.8	485.03	400.75	1.795	1.483	408.01	316.74	1.510	1.1724
2	593.66	506.63	1.780	1.519	497.38	404.07	1.491	1.2115

The maximum value of the drag coefficient for an ellipsoid is at a flow velocity of 1.2 Mach and for a short elliptical cylinder, the drag coefficient is maximum for a flow velocity of 1.5 Mach. A short elliptical cylinder has a higher wave drag coefficient than an ellipsoid for the same flow velocity and that difference is between 28.2% for $M = 2$ and 59.9% for $M = 1$.

Parallelepiped, for the chosen flow velocities, has a maximum drag coefficient at a flow velocity of 1.5 Mach, and the long elliptic cylinder has a maximum drag coefficient for $M = 1.2$. Wave drag coefficient is higher for parallelepiped than for long elliptic cylinder, with a difference between 25.4% for $M = 2$ and 48.1% for $M = 1$. At $M = 1$, the wave drag coefficient is about 49% of the drag coefficient for bodies with a rounded front surface and more than 63% for bodies with a flat front surface. At $M = 1.5$ this ratio is higher and ranges from 70% to 77%, and for $M = 2$ from 80% to 85%. The largest drag force has parallelepiped at $M = 2$ which is a consequence of the maximum wave drag coefficient.

Although all the bodies have the same dimensions, the most favorable shape from an aerodynamic view (minimum drag coefficient) is ellipsoid. Pressure distribution on the front surface of the ellipsoid, short elliptic cylinder, long elliptic cylinder, and parallelepiped for $M = 1$ is shown in Fig. 4, and for $M = 1.5$ the pressure distribution is shown in Fig. 5. The pressure range is the same in all pictures of pressure distribution on the bodies.

Ellipsoid and short elliptic cylinders have the same maximum cross-section area which is taken as the referent area and for which the drag coefficient is determined.

The front surface of the ellipsoid is curved and the front surface of the short elliptic cylinder is flat and they are perpendicular to the airflow. Ellipsoid has no discontinuity of the outer surface and for a short elliptic cylinder, the angle between the front surface and the rest of the wet surface is 90° (surface discontinuity).

The area of the ellipsoid's front surface which is exposed to the maximum pressure is smaller than the area of the short elliptic cylinder's front surface which is affected by the same pressure. At the outer boundary of the ellipsoid's front surface, pressure is lower than the pressure on the edge of the short elliptic cylinder's front surface.

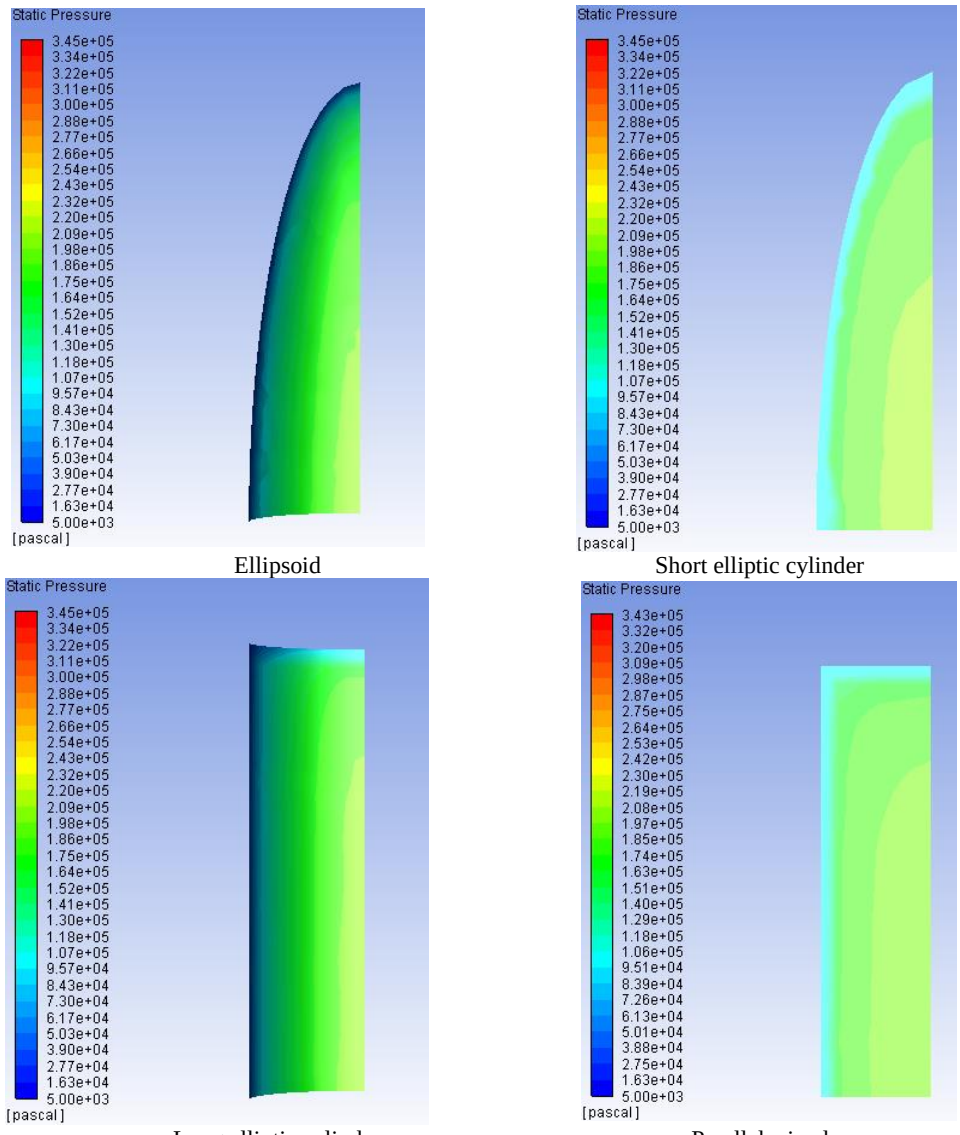

Fig. 4: Pressure distribution on the front surface of the ellipsoid, short elliptic cylinder, long elliptic cylinder, and parallelepiped for $M = 1$

For parallelepiped and long elliptic cylinders, the area of the maximum cross-section is the same. On the curved part of the long elliptic cylinder's outer boundary, pressure is lower than on the sharp edges. The pressure is the same at all points of the parallelepiped's edge. Also, the area of the parallelepiped's front surface, where maximum pressure is acting, is bigger than the one of the long elliptic cylinder's front surface.

At $M = 1$ maximum pressure acting on the front surface of the body is 1.89 times greater than the pressure of air free flow. At $M = 1.5$ maximum pressure is 3.41 times greater than the pressure of air free flow and at $M = 2$ the pressure is 5.64 times greater than the pressure of air free flow.

For $M = 1$, the velocity flow field as the contour of Mach number around the ellipsoid, short elliptic cylinder, long elliptic cylinder, and parallelepiped on the length-width plane of the body is shown in Fig. 6.

On the length-high plane of the body, the velocity flow field as the contour of Mach number around the ellipsoid, short elliptic cylinder, long elliptic cylinder, and parallelepiped for $M = 1$ is shown in Fig. 7.

The normal shock wave is generated far out in front of the body and a large subsonic region ($M < 1$) is formed between the shock wave and the front surface of the body.

For a velocity of 1.5 Mach, the flow field as the contour of Mach number around ellipsoid, short elliptic cylinder, long elliptic cylinder, and parallelepiped on length-width of body plane is shown in Fig. 8.

On length-high of the body plane, the velocity flow field as the contour of Mach number around ellipsoid, short elliptic cylinder, long elliptic cylinder, and parallelepiped for $M = 1.5$ is shown in Fig. 9.

The same range of Mach number, from 0 to 2.53, was used for Figs. 6 and 7 showing the velocity flow field as the contour of the Mach number.

By comparing Figs. 6 and 7 of flow around ellipsoid and short elliptic cylinder, which both have the same shape and area of cross-section, and long elliptic cylinder and parallelepiped, which have a rectangular cross-section of the same size (maximum cross-section), it is noticed that the distance between the front of the detached bow

shock and the front surface of the body is bigger in cases where the air flows around a flat surface.

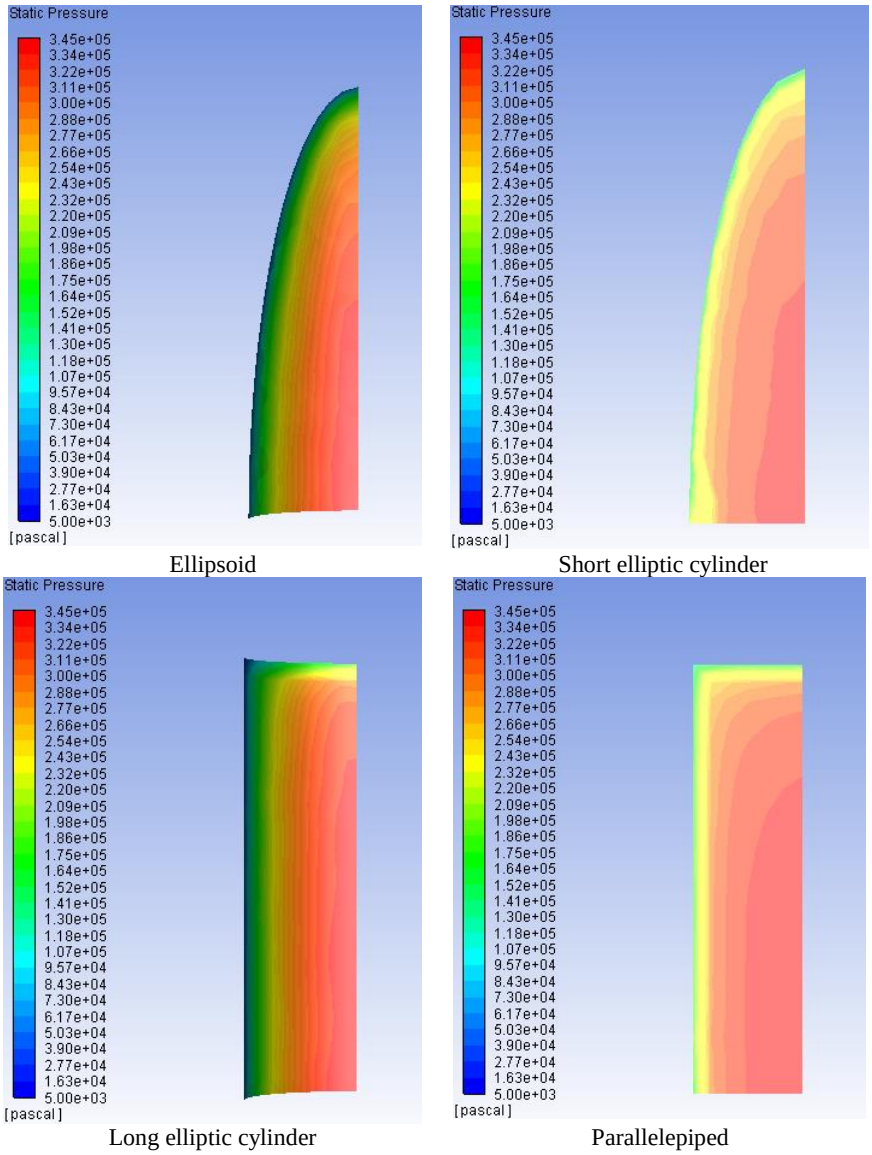

Ellipsoid Short elliptic cylinder

Long elliptic cylinder Parallelepiped

Fig. 5: Pressure distribution on the front surface of the ellipsoid, short elliptic cylinder, parallelepiped, and long elliptic cylinder for $M = 1.5$

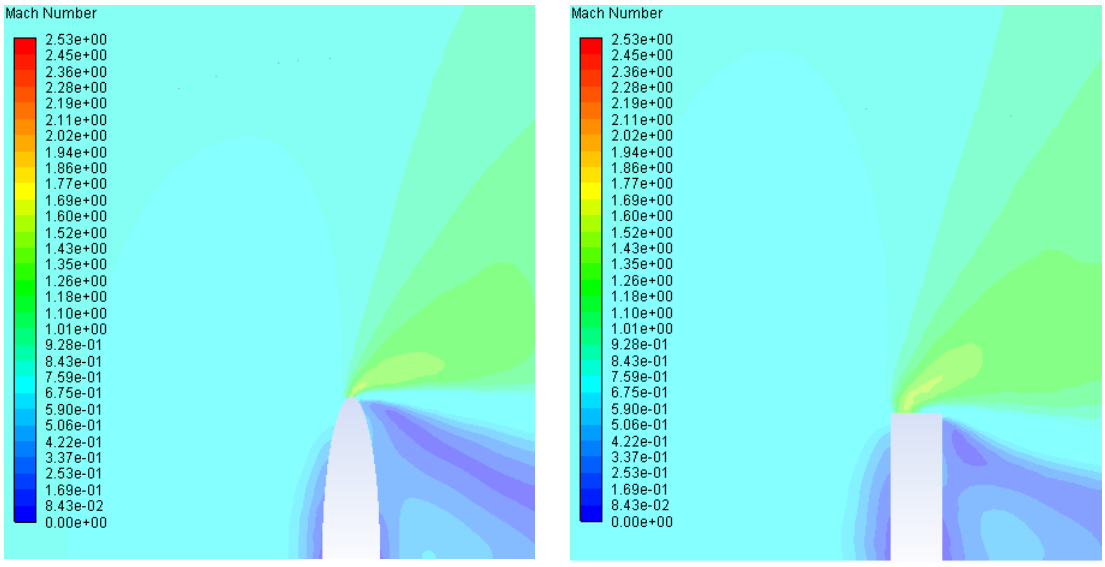

Ellipsoid Short elliptic cylinder

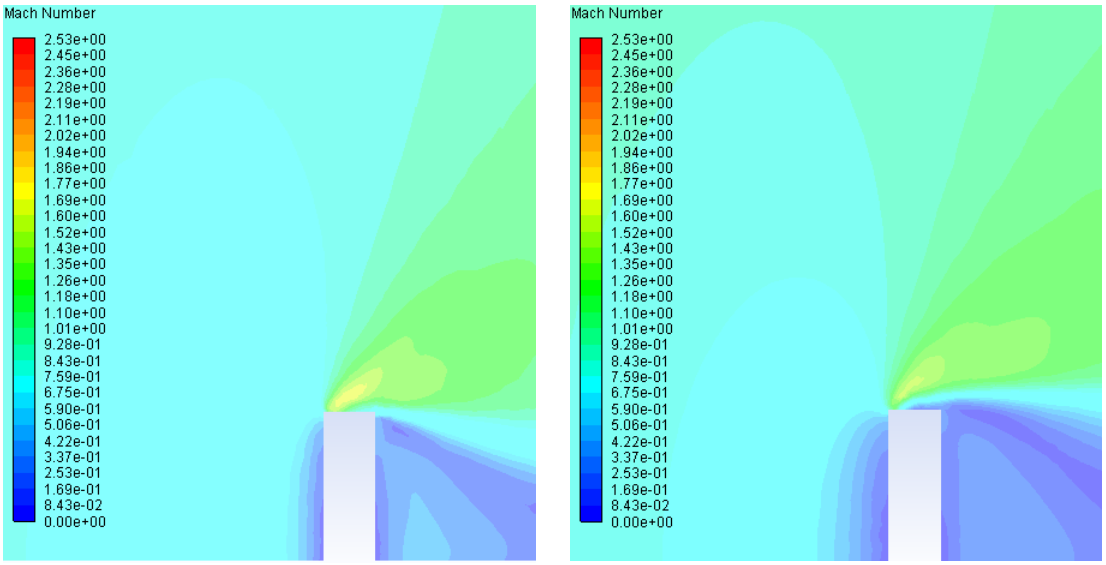

Long elliptic cylinder Parallelepiped

Fig. 6: Velocity flow field around bodies as the contour of Mach number (length-width plane of the body), for $M = 1$

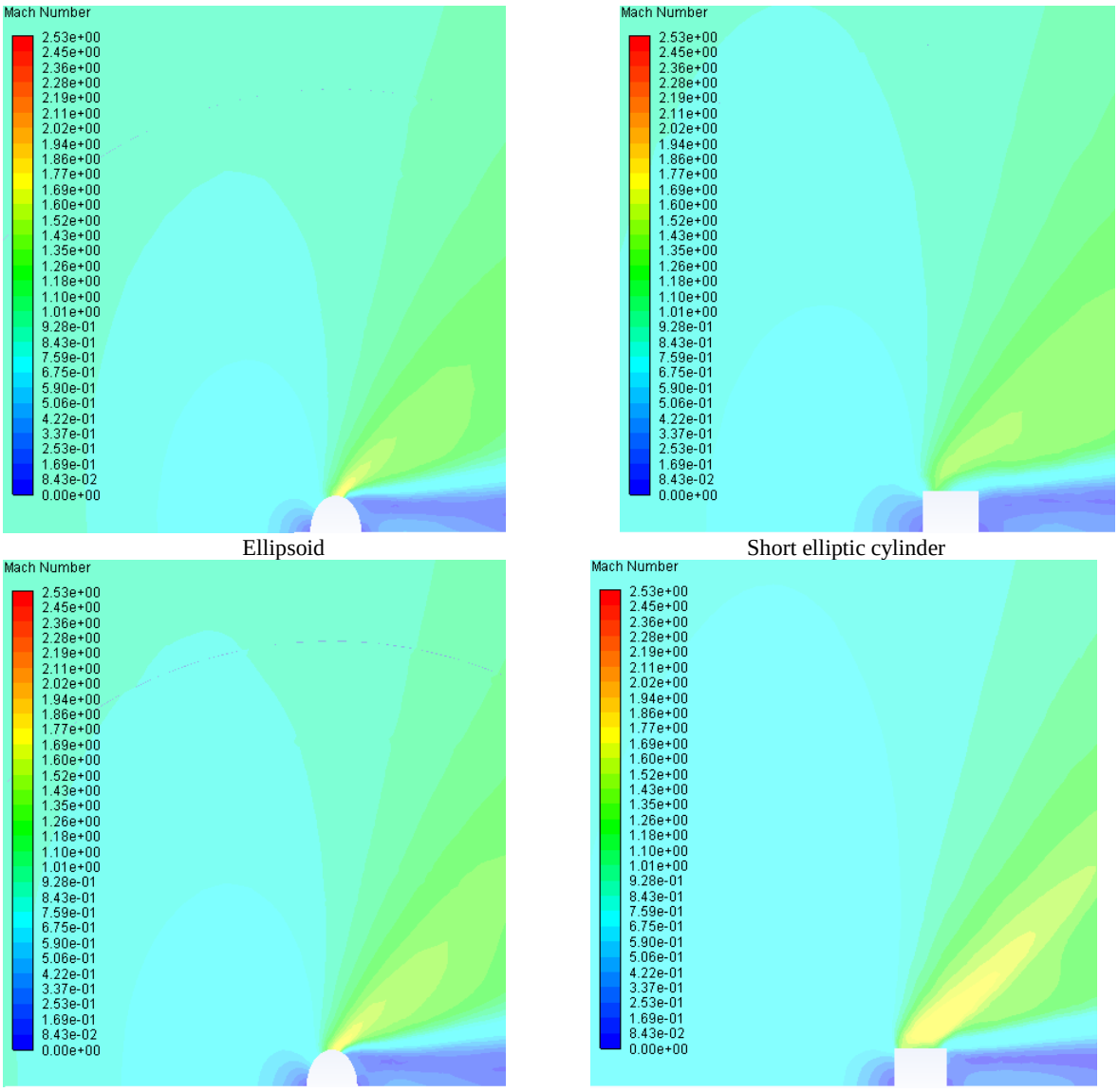

Ellipsoid Short elliptic cylinder

Long elliptic cylinder Parallelepiped

Fig. 7: Velocity flow field around bodies as the contour of Mach number (length-high plane of the body), for $M = 1$

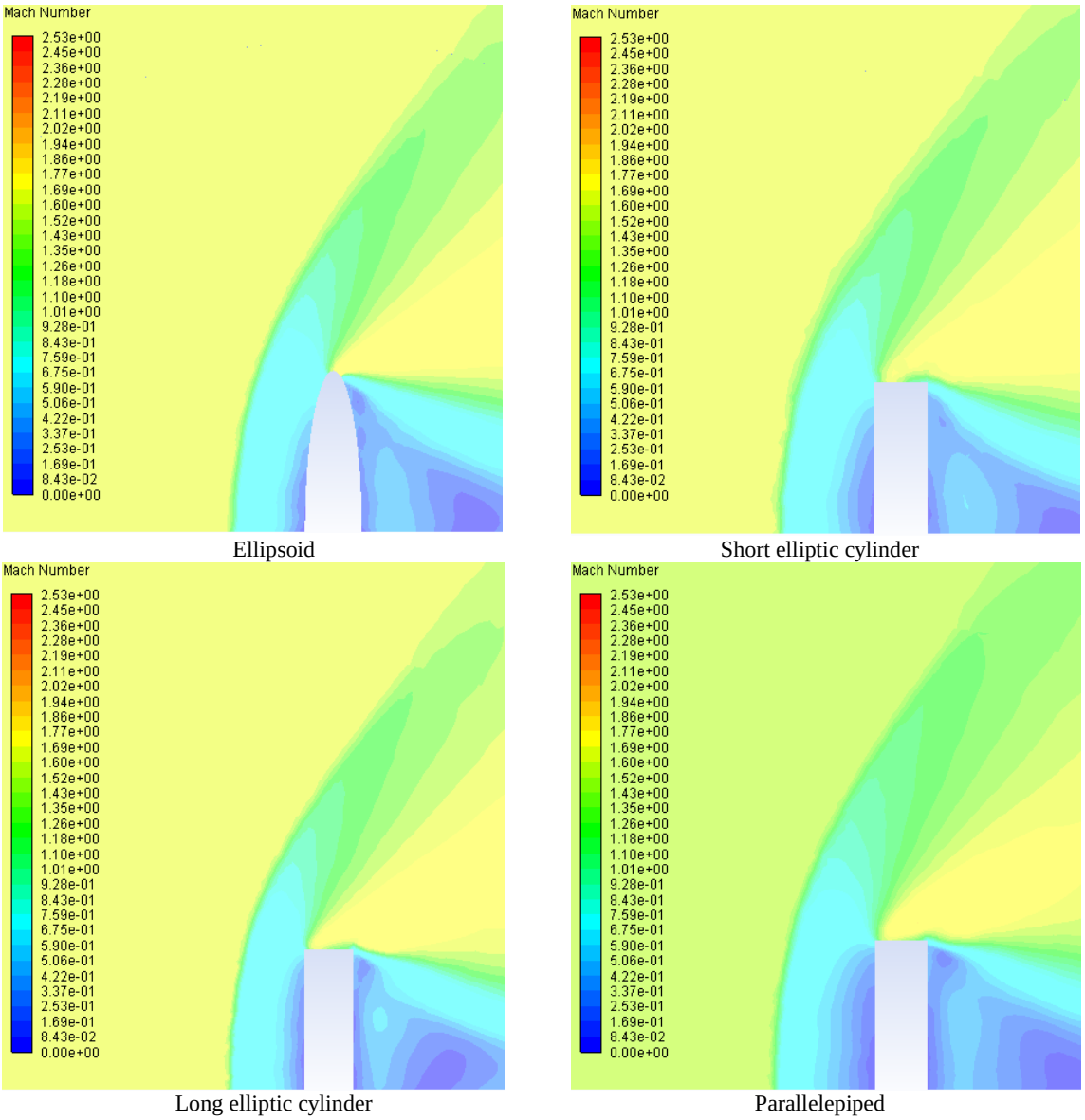

Ellipsoid | Short elliptic cylinder

Long elliptic cylinder | Parallelepiped

Fig. 8: Velocity flow field around bodies as the contour of Mach number (length-width plane of the body), for $M = 1.5$

The curvature radius of the detached bow shock wave when the air flows around the flat front surface is greater than the curvature radius of the detached bow shock wave when the air flows around the rounded front surface.

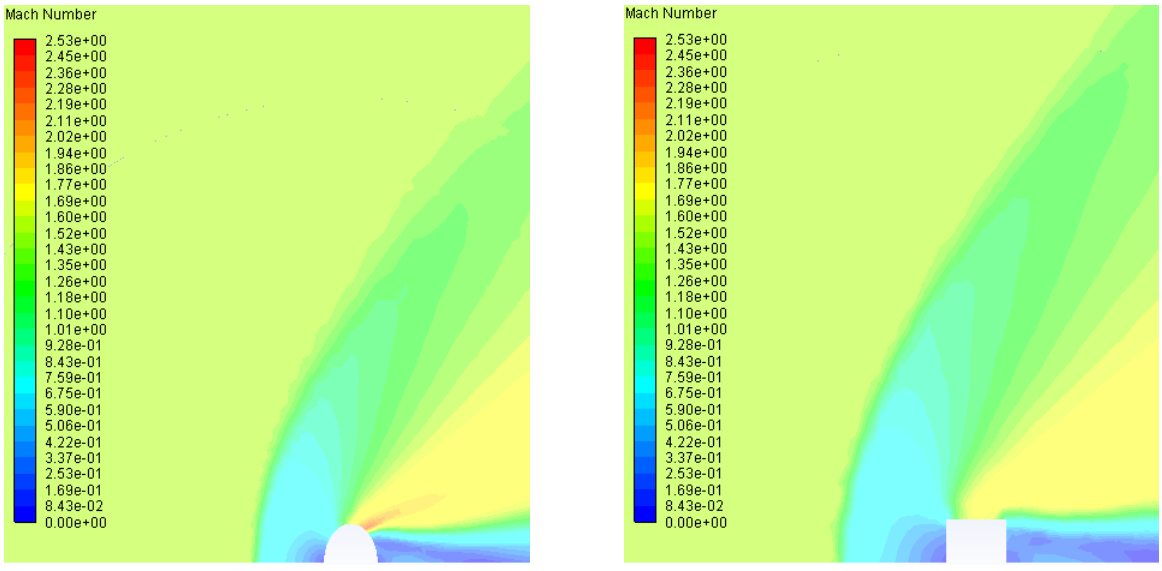

Ellipsoid | Short elliptic cylinder

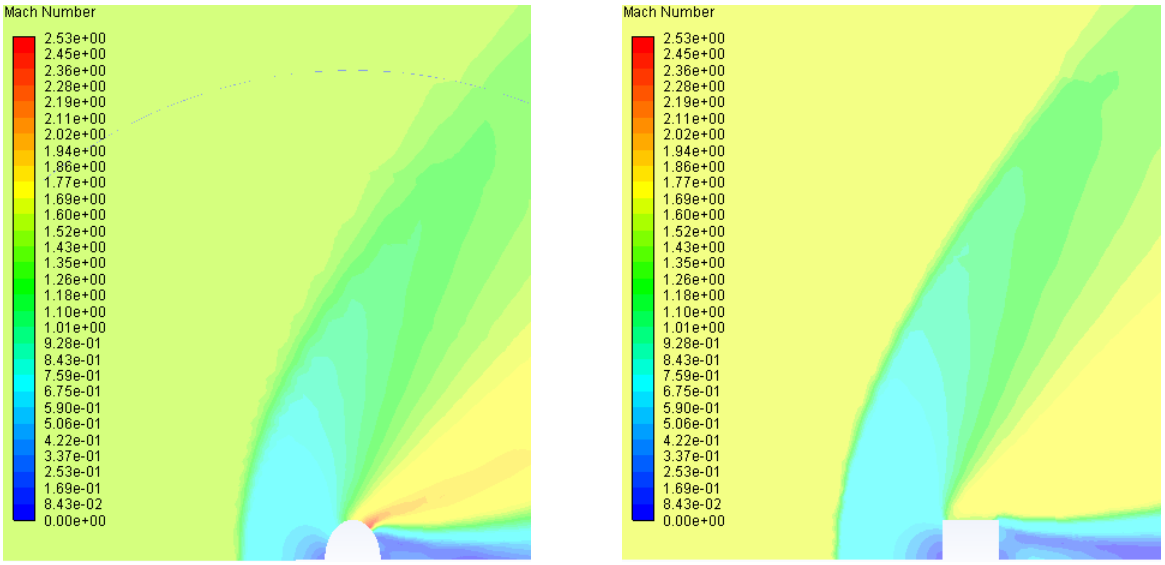

Long elliptic cylinder Parallelepiped

Fig. 9: Velocity flow field around bodies as the contour of Mach number (length-high plane of the body), for $M = 1.5$

5. Conclusion

Four series of numerical computations were made for irregular-shaped bodies at transonic and supersonic speeds, $1 \leq M \leq 2$. Bodies with the same width, high and length, and different shapes (ellipsoid, short elliptic cylinder, long elliptic cylinder, and parallelepiped) were chosen. Ellipsoid and short elliptic cylinders have cross-section areas in the shape of an ellipse and long elliptic cylinders and parallelepiped have cross-section areas in the shape of a rectangle. The front surface of the ellipsoid and long elliptic cylinder is rounded and the front surface of the short elliptic cylinder and parallelepiped is flat.

Drag coefficient and wave drag coefficient were analyzed with respect to flow velocity and front surface curvature of the body.

An Ellipsoid has minimum drag coefficient and a parallelepiped has maximum drag coefficient at transonic and supersonic regimes.

It was confirmed that the front surface curvature of the body at transonic and supersonic speeds has a significant influence on to wave drag coefficient and therefore the total drag coefficient of the body. The influence is related to detached shock wave distance. The aerodynamic drag coefficient of the body is lower in the case of a curved front surface than in the case of a flat front surface. The shape of the outer edge of the flat front surface (elliptic or rectangular) does not affect the wave drag coefficient, and the shape of the outer edge of the curvature front surface has a small influence on to wave drag coefficient.

It was confirmed that the wave drag coefficient made up the largest part of the drag coefficient at high speeds and it grows with the increase of Mach number. The influence of the curvature of the front surface on the share of wave drag coefficient in the total drag coefficient decreases with increasing Mach number.

Follow-up research should deal with the analysis of the rear (base) drag coefficient of an irregular-shaped body at transonic speeds because it is a significant part of the drag coefficient at $M \approx 1$.

List of symbols

A_{ref}	Reference area
C_D	Drag coefficient
C_{D_r}	Pressure drag coefficient due to dry surface
$C_{D_{sf}}$	Skin friction drag due to wet surface
C_{D_w}	Pressure drag coefficient due to wet surface
D	Drag force
D_w	Wave drag force
M	Mach number
p	Pressure behind the normal shock wave
p_∞	Freestream pressure
p_0	Stagnation pressure
S_d	Dry surface
S_w	Wet surface
V_∞	Freestream velocity
ρ_∞	Freestream density

Compliance with ethical standards

Conflict of interest

The author(s) declared no potential conflicts of interest with respect to the research, authorship, and/or publication of this article.

References

Anderson JD (2017). Fundamentals of aerodynamics. 6th Edition, McGraw-Hill Editions, New York, USA.

Catovic A, Kljuno E, and Voloder A (2018). Analysis of flow around high speed irregularly shaped bodies using numerical simulations. International Journal of Advanced and Applied

Sciences, 5(8): 1-10.
https://doi.org/10.21833/ijaas.2018.08.001

Kljuno E and Catovic A (2019). A generalized model for estimation of aerodynamic forces and moments for irregularly shaped bodies. Defence Technology, 15(3): 369-389.
https://doi.org/10.1016/j.dt.2018.09.006

McCleskey F (1988). Drag coefficients for irregular fragments. Final Report No. NSWC-TR-87-89, Naval Surface Warfare Center Dahlgren, Dahlgren, USA.
https://doi.org/10.21236/ADA201943

Miller MC (1990). Drag coefficient measurements for typical bomb and projectile fragments. Army Research Development and Engineering Command Aberdeen Proving Ground, Maryland, USA.

Moore F (2000). Approximate methods for weapon aerodynamics. American Institute of Aeronautics and Astronautics Inc., Reston, USA. https://doi.org/10.2514/4.473999

Moxnes JF, Frøyland Ø, Øye IJ, Brate TI, Friis E, Ødegårdstuen G, and Risdal TH (2017). Projected area and drag coefficient of high velocity irregular fragments that rotate or tumble. Defence Technology, 13(4): 269-280.
https://doi.org/10.1016/j.dt.2017.03.008

Murman SM (2010). Lift and drag behavior of unconstrained bluff bodies. NASA TM-216406, National Aeronautics and Space Administration, Washington, USA.

Spalart P and Allmaras S (1992). A one-equation turbulence model for aerodynamic flows. In the Proceedings of the 30th Aerospace Sciences Meeting and Exhibit, Reno, NV, USA.
https://doi.org/10.2514/6.1992-439

Twisdale LA and Vickery PJ (1992). Comparison of debris trajectory models for explosive safety hazard analysis. In the 25th DoD Explosive Safety Seminar, Anaheim, USA: 18-20.